Characterizing Crustal Earthquake Slip Models for the Prediction of Strong Ground Motion

by Paul Somerville, Kojiro Irikura, Robert Graves, Sumio Sawada, David Wald, Norman Abrahamson, Yoshinori Iwasaki, Takao Kagawa, Nancy Smith, and Akira Kowada

Characterizing Crustal Earthquake Slip Models for the Prediction of Strong Ground Motion

Paul Somerville
Woodward-Clyde Federal Services

Kojiro Irikura
Disaster Prevention Research Institute, Kyoto University, Japan

Robert Graves
Woodward-Clyde Federal Services

Sumio Sawada
Disaster Prevention Research Institute, Kyoto University, Japan

David Wald
United States Geological Survey

Norman Abrahamson
Pacific Gas & Electric Company, San Francisco

Yoshinori Iwasaki
Takao Kagawa
GeoResearch Institute, Japan

Nancy Smith
Woodward-Clyde Federal Services

Akira Kowada
Kansai Electric Power Co., Japan

INTRODUCTION

A large amount of work has been done in recent years to estimate the distribution of slip on the fault surface during earthquakes. Generally, these slip models are derived from longer period ground motions: strong-motion velocity and displacement, and teleseismic velocity seismograms. At these longer periods, ground motions are predominantly deterministic and their waveforms can in general be accurately modeled using simple descriptions of the source and crustal structure. The opposite situation exists for the prediction of high-frequency strong ground motions. Ground motions at high frequencies are predominantly stochastic, and their waveforms in general cannot be accurately modeled using simple descriptions of the source and crustal structure. However, preliminary evidence (e.g., Hartzell et al., 1996; Kamae and Irikura, 1998; Somerville, 1993; Somerville et al., 1996; Wald et al., 1988) suggests that variable slip models derived from longer-period ground-motion recordings are relevant for the prediction of higher-frequency ground motions. For both short and long periods, one of the main uncertainties in the prediction of strong ground motion is the uncertainty in specifying the appropriate methods of characterizing the source characteristics of future earthquakes. The objective of this paper is to develop information for characterizing the slip models of future earthquakes for use in the prediction of strong ground motion.

TABLE 1
Source Parameters of Crustal Earthquakes

Earthquake, Location	Date	Mech.	$M_o \times 10^{25}$ dyne-cm	M_w	Slip Duration (sec)	Rupture Velocity (km/sec)
Landers, California	1992.6.28	SS	.75	7.22	2.0	2.7
Tabas, Iran	1978.9.16	RV	58	7.14	2.1	2.5
Loma Prieta, California	1989.10.17	OB	30	6.95	1.5	2.7
Kobe, Japan	1995.1.17	SS	24	6.9	2.0	2.8
Borah Peak, Idaho	1983.10.28	NM	23	6.87	0.6	2.9
Nahanni, N.W.T., Canada	1985.12.23	RV	15	6.75	2.5	2.75
Northridge, California	1994.1.17	RV	11	6.66	1.25	3.0
Nahanni, N.W.T., Canada	1985.10.05	RV	10	6.63	0.75	2.75
San Fernando, California (Sierra Madre)	1971.2.9	RV	7	6.53	0.8	2.8
Imperial Valley, California	1979.10.15	SS	5	6.43	0.7	2.6
Superstition Hills, California (event #3)	1987.11.24	SS	3.5	6.33	0.5	2.4
Morgan Hill, California	1984.4.24	SS	2.1	6.18	0.3	2.8
North Palm Springs, California	1986.8.7	OB	1.8	6.14	0.4	3.0
Whittier Narrows, California	1987.10.1	RV	1	5.97	0.3	2.5
Coyote Lake, California	1979.6.8	SS	0.35	5.66	0.5	2.8

An important aspect of the problem of characterizing the earthquake source is the degree of fault heterogeneity or roughness. The heterogeneity may be manifested as local variations in static slip, slip velocity, or rupture velocity. It is possible that all three are interdependent and that each contributes significantly to the high-frequency radiation. There is little agreement, however, in exactly how these characteristics are physically related. In most broadband strong-motion simulation procedures (*e.g.*, Somerville *et al.*, 1996), the spatial variations in slip are modeled in a deterministic manner because they are fairly well constrained by data. Variations in rupture velocity and slip velocity are usually modeled in a stochastic manner because at present it is difficult to constrain these variations in a deterministic manner. However, we can include deterministic variations in rupture velocity and slip velocity when enough information becomes available to constrain them. Accordingly, this paper focuses on characterizing the spatial variation of slip on the fault. The slip models of shallow crustal earthquakes are characterized by strong spatial variation in slip on the fault surface, including asperities (which we define as regions of large slip on the fault).

In the following sections, we describe analyses of the characteristics of slip models of fifteen crustal earthquakes. Except for the 1978 Tabas and 1995 Kobe earthquakes, all of the earthquakes occurred in western North America. The slip models were derived in a fairly uniform manner from the inversion of lowpass-filtered near-source strong-motion recordings and teleseismic body waves. We quantify the characteristics of asperities of individual earthquakes and examine their average characteristics. We then examine how the slip models scale with seismic moment. We also use the spatial wavenumber spectrum as an additional method of describing the heterogeneity of slip on the fault surface.

SLIP MODELS

The slip models of past earthquakes show that the spatial variation of slip (and seismic wave radiation) over the fault surface is an important aspect of the earthquake source. Summaries of slip models of these earthquakes are given by Mendoza and Hartzell (1988b) and Heaton (1990). Enough slip models have been derived over the past twenty years that we can now examine their systematic features. We can then use these systematic features to generate slip models for the prediction of strong ground motion.

The earthquakes analyzed in this study are listed in Table 1. All fifteen of these crustal earthquakes have rupture models in which the slip varies spatially over the fault surface. The orientation of the fault planes and reference to the slip model used are given in Table 2, and the dimensions and discretization of the fault planes are given in Table 3.

In this study, we use a rectangular representation of the fault rupture because our objective is to develop methods of generating slip models on rectangular fault planes. In most slip model inversions, the rectangular dimensions of the fault are chosen to be at least large enough to accommodate the entire fault rupture, and so they generally overestimate the actual dimensions of the rupture area. Accordingly, we

TABLE 2.
Orientation of Fault Planes

Earthquake	depth of top (km)	depth of bottom (km)	dip	strike	slip model reference
Landers	0.0	15.0	90°	355° 334° 320°	Wald et al., 1994
Tabas	1.0	20.0	25°	330°	Hartzell & Mendoza, 1991
Loma Prieta	3.4	20.3	70°	128°	Somerville et al., 1993; Wald et al., 1991
Kobe: Nojima Suma/Suwayama	0.2 0.2	20.0 20.1	80° 85°	45° 230°	Wald, 1996
Borah Peak	1.0	20.9	49°	152°	Mendoza & Hartzell, 1988a
Nahanni (85/12/23)	2.0	9.0	25°	160°	Hartzell et al., 1994
Northridge	5.0	21.4	40°	122°	Wald et al., 1994
Nahanni (85/10/05)	0.2	8.2	35°	160°	Hartzell et al., 1994
San Fernando (SM)	3.0	12.7	54°	290°	Heaton, 1982
Imperial Valley	0.0	10.0	90°	143°	Hartzell & Heaton, 1983
Superstition Hills (#3)	3.95	12.0	90°	127°	Wald et al., 1990
Morgan Hill	0.5	12.0	90°	148°	Hartzell & Heaton, 1986
North Palm Springs	4.0	13.63	46°	287°	Hartzell, 1989
Whittier Narrows	12.1	17.1	30°	280°	Hartzell & Iida, 1990
Coyote Lake	3.5	9.5	80°	336°	Liu & Helmberger, 1983

TABLE 3.
Dimensions and Discretization of Fault Planes*

Earthquake	T	B	L	R	length (km)	width (km)	nx	ny	dx (km)	dy (km)	kx_{max} (km^{-1})	ky_{max} (km^{-1})
Landers			1	2	69.0	15.0	23	6	3.0	2.5	0.167	0.2
Tabas					95.0	45.0	21	10	4.52	4.5	0.111	0.111
Loma Prieta	1				40.0	18.0	20	9	2.0	2.0	0.25	0.25
Kobe					60.0	20.0	18	8	3.33	2.5	0.15	0.2
Borah Peak			1		48.75	26.4	15	8	3.25	3.3	0.154	0.152
Nahanni (12/23)		2	2	3	34.67	16.49	13	7	2.67	2.36	0.187	0.212
Northridge					18.0	21.0	14	14	1.29	1.5	0.386	0.333
Nahanni (10/05)		2	2	2	29.33	13.92	11	8	2.67	1.74	0.187	0.287
San Fernando (Sierra Madre)		2	1	1	13.36	12.03	5	9	2.67	1.33	0.187	0.375
Imperial Valley			1		36.0	10.0	12	4	3.0	2.5	0.167	0.2
Superstition Hills (event 3)	3				20.0	8.05	20	7	1.0	1.15	0.5	0.435
Morgan Hill				1	26.0	11.5	26	6	1.0	1.92	0.5	0.26
North Palm Springs		1		1	20.0	13.3	10	7	2.0	1.9	0.25	0.263
Whittier Narrows					10.0	10.0	10	10	1.0	1.0	0.5	0.5
Coyote Lake	2	2	2	2	5.5	4.57	11	12	0.5	0.38	1.0	1.312

*T, B, L, and R in the first four columns refer to the numbers of rows trimmed from the top (T) and bottom (B) of the slip model, and from the left side (L) and right side (R) of the slip model.
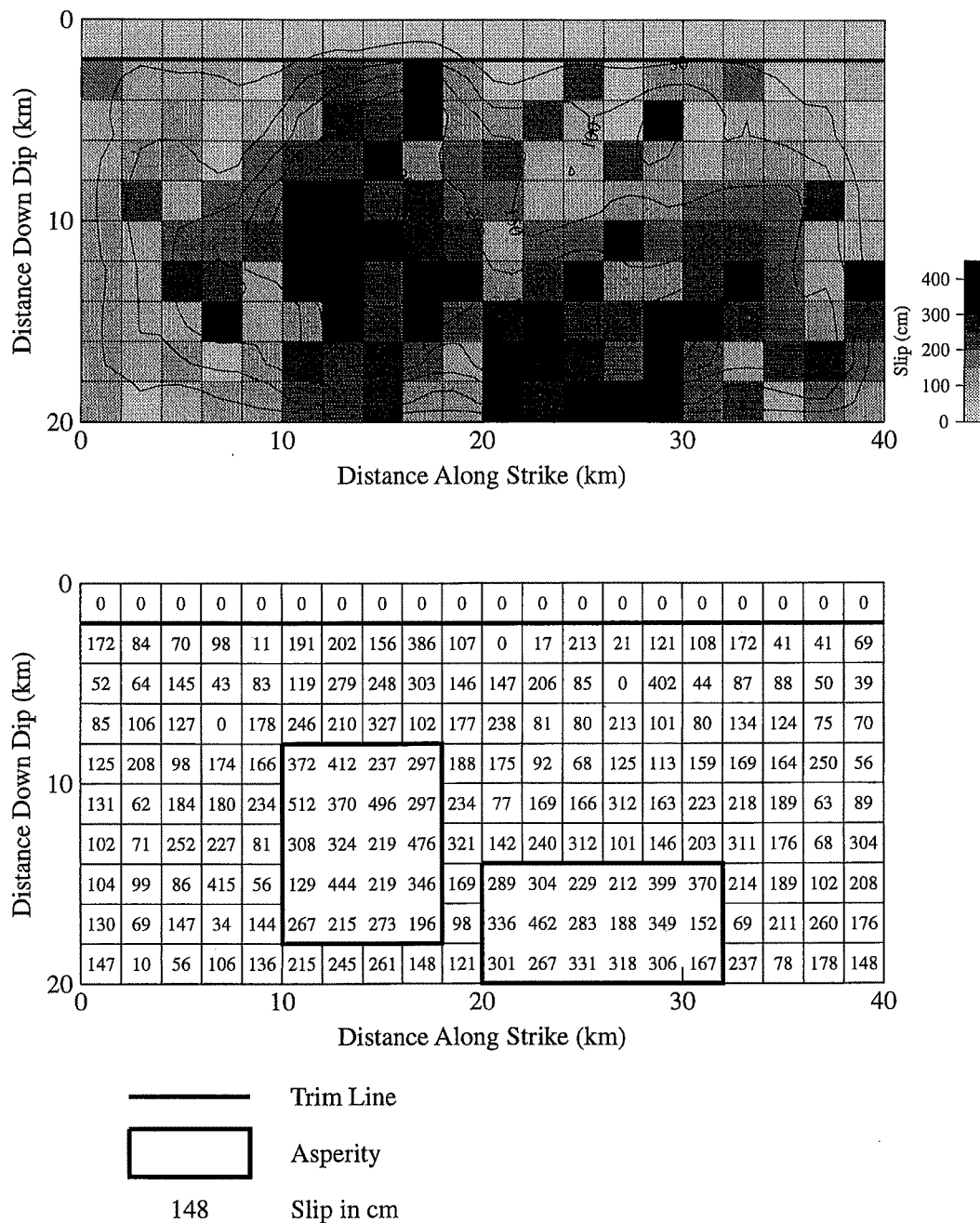
▲ **Figure 1.** Slip model of the 1989 Loma Prieta, California earthquake (Somerville *et al.*, 1994, based on Wald *et al.*, 1991) and identification of asperities on it.

reduced the dimensions of the rectangular fault slip models using a standard criterion for trimming the edges of the slip models. The criterion is that an edge row or column of the slip model is removed if the average slip per fault element in the entire row or column is less than 0.3 times the average slip of the whole fault. The edge row or column that has the lowest slip per fault element is removed first, and then the process is repeated until all edge rows and columns have normalized average slip per fault element of 0.3 or larger. The trimming of each event is documented in Table 3. The trimmed fault defines the rupture area used in this study. As

an example, the slip model of the 1989 Loma Prieta earthquake is shown in Figure 1.

The slip duration (or dislocation rise time) determined from the inversion of each event is shown in Table 1. The rise time was based on the time-window length for the five events having a single time window and on an assessment of the predominant rise time for the ten events having multiple time windows. This parameter has a direct influence on the amplitudes of high-frequency ground motions: the shorter the slip duration, the larger the ground motions. Heaton (1990) showed that the slip duration is short relative to the

rupture time. In a later section, we derive an empirical relation between the slip duration and the seismic moment.

Heaton (1982) derived a slip model of the 1971 San Fernando earthquake that involves slip on two separate rupture planes. In this study, we concentrate on the deeper (Sierra Madre) rupture plane because the slip model of the shallower (San Fernando) rupture plane may not be accurate at shallow depths (Vidale and Helmberger, 1988). Wald et al. (1990) derived a slip model of the 1987 Superstition Hills earthquake that has three spatially overlapping subevents. We analyze only the third and largest subevent.

DISTRIBUTION OF SLIP AND SEISMIC MOMENT RELEASE WITH DEPTH

One of the most important aspects of slip models is the variation of slip with depth. We expect this depth dependence of slip to be a systematic feature of earthquakes on a given fault or fault system, since it is presumably controlled by the dependence of rock rheology on depth. We expect that the variation of slip along strike may be controlled by geometrical factors such as fault bends or lateral changes in rock type and that these variations may be more random than variations with depth.

For this analysis, we divide the earthquakes into three categories: strike-slip, oblique, and dip-slip. The distribution of slip and moment release with depth for individual events within each of these categories are shown in Figure 2. The slip and the seismic moment release in these figures are averages per km of fault length along strike. The seismic moment release is proportional to the product of slip and shear modulus.

The distribution of slip with depth for the six strike-slip earthquakes is characterized by a very large degree of variability. Slip was concentrated at shallow depths in the Landers earthquake, was distributed uniformly with depth in the Kobe earthquake, and was concentrated in the depth range of 5 to 12 km in the 1979 Imperial Valley and 1987 Superstition Hills earthquakes. Both of the latter two earthquakes occurred in or on the margins of a sedimentary basin that is about 5 km thick, suggesting that seismic radiation may be confined mostly to regions of the fault where there is crystalline rock on both sides.

The two oblique earthquakes occurred on regions of the San Andreas Fault system where a regional bend in fault strike produces a dipping fault and a combination of strike-slip and reverse-slip motion. These are the 1986 North Palm Springs earthquake and the 1989 Loma Prieta earthquake. The deepest depth of slip for these events is significantly greater than that for the strike-slip faults in California, and the slip generally increases with depth down to at least 10 km.

The one normal faulting and six thrust earthquakes are from a wide range of faulting environments. Although they have rather different slip distributions with depth, there is a tendency for slip on some reverse faults to decrease with depth below about 5 km, rather than increase as is the case for the

Strike-slip Events

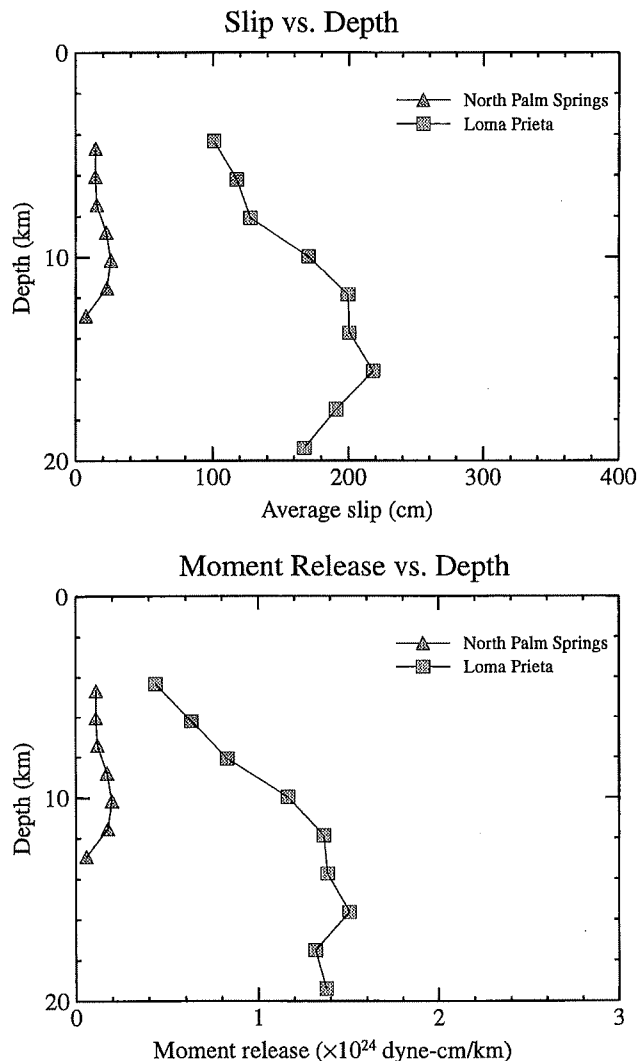### Slip vs. Depth

Moment Release vs. Depth
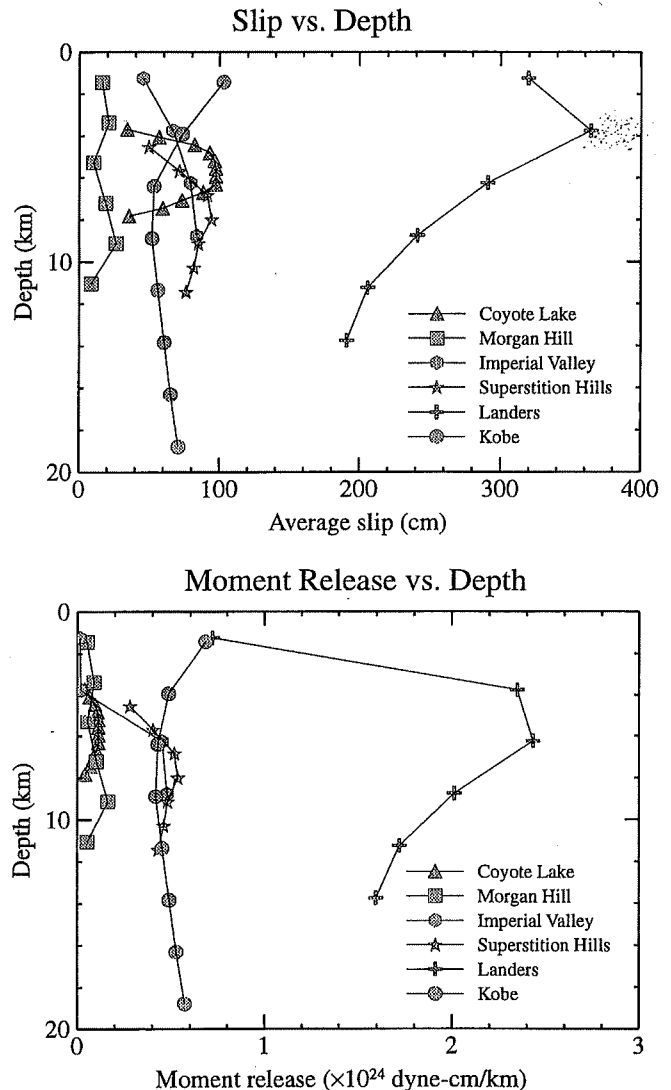
▲ **Figure 2(A).** Distribution of average slip and average seismic moment release per km of rupture length as a function of depth for strike-slip earthquakes.

oblique earthquakes. However, the Northridge earthquake, which was a blind thrust event, has slip concentrated at depth. The slip distribution of the Borah Peak earthquake, which is a normal faulting event, is relatively uniform with depth.

ANALYSIS OF FAULT ASPERITIES

An asperity is a region on the fault rupture surface that has large slip relative to the average slip on the fault. For the purposes of this study, we have defined an asperity as a rectangular region in which the slip exceeds, in a specified way, the slip averaged over the entire fault rupture. We chose a rectangular definition of asperities to facilitate the generation of slip models of future earthquakes using this simple geometry.
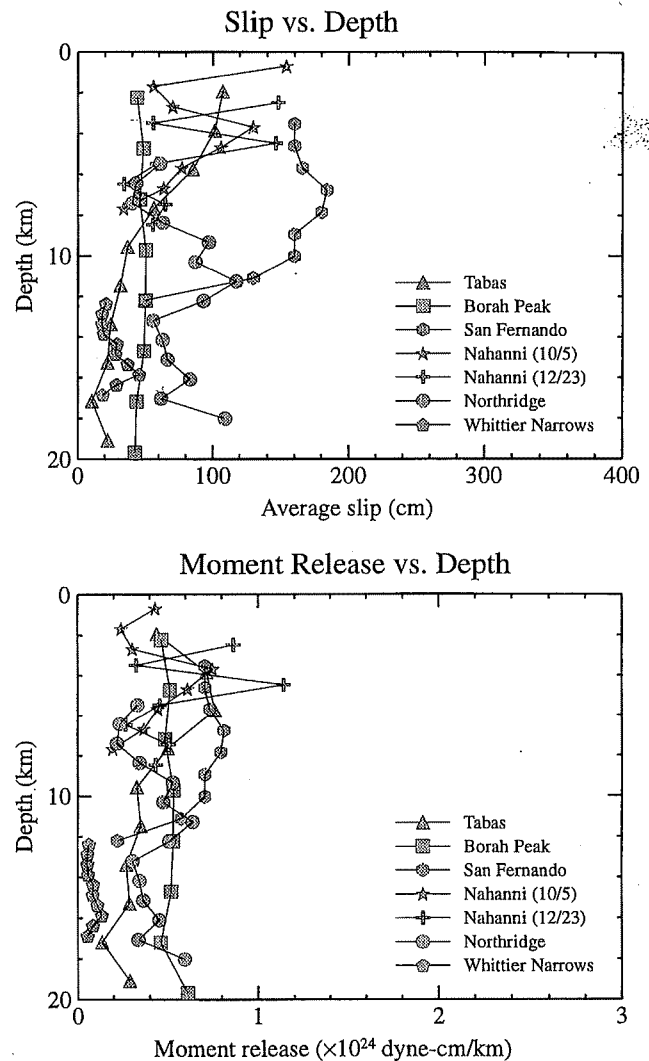
Oblique-slip Events

Slip vs. Depth

Moment Release vs. Depth

▲ **Figure 2(B).** Distribution of average slip and average seismic moment release per km of rupture length as a function of depth for oblique-slip earthquakes.

Dip-slip Events

Slip vs. Depth

Moment Release vs. Depth

▲ **Figure 2(C).** Distribution of average slip and average seismic moment release per km of rupture length as a function of depth for dip-slip earthquakes.

An asperity is initially defined to enclose fault elements whose slip is 1.5 or more times larger than the average slip over the fault and is subdivided if any row or column has an average slip less than 1.5 times the average slip. The asperity is then trimmed until all of the edges have an average slip equal to or larger than 1.25 times the slip averaged over the entire rupture area. The discretization of the fault into fault elements places limits on the size of the smallest asperity. In view of this discretization, we require an asperity to have a minimum of two elements if the slip of each is 2 or more times the average slip, and a minimum of four elements if the slip of each is 1.5 or more times the average slip, or the slip of one is 2 or more and the slip of two others is 1.5 or more times the average slip. We apply this definition of an asperity to the fifteen slip models described above. As an

example, the asperities for the slip model of the 1989 Loma Prieta earthquake are shown at the bottom of Figure 1.

The number of asperities in the slip models of the fifteen events ranges from one to six. In Tables 4 and 5, we list each parameter of the individual asperities for each of the events. In Table 4 we list the asperity's area, its area as a fraction of the overall rupture area (called the area ratio), its average slip, its average slip as a fraction of the average slip of the overall rupture (called the slip ratio), its average distance from the hypocenter, and its average rupture time relative to the origin time. In Table 5, we list its length and width, both absolute and normalized to the length and width of the fault, respectively, and its horizontal and down-dip distance from the "left" top corner of the fault (from which the fault strike is positive), both absolute and normalized to the length and width of the fault.

Earthquake	Asp. #	Area of Asperity (km²) abs	Area of Asperity (km²) norm	Avg. Slip (cm) abs	Avg. Slip (cm) norm	Hypo. Dist. (km)	Rupt. time (sec)
Landers	1	67.5	0.065	471.1	1.75	46.70	17.29
	2	180.0	0.174	498.9	1.86	33.28	12.32
	3	45.0	0.043	513.0	1.91	15.59	5.77
Tabas	1	122.1	0.029	92.52	1.86	20.57	8.23
	2	40.71	0.095	141.7	2.84	18.48	7.39
	3	814.3	0.190	122.348	2.45	24.33	9.73
	4	61.07	0.014	102.47	2.06	43.26	17.3
	5	81.43	0.019	87.23	1.75	53.94	21.57
Loma Prieta	1	80.0	0.11	307.0	1.85	7.75	2.87
	2	72.0	0.10	270.1	1.63	6.32	2.34
Kobe	1	33.3	0.028	121.93	1.83	22.47	8.02
	2	266.7	0.222	125.8	1.88	11.20	4.00
Borah Peak	1	514.8	0.40	75.62	1.62	17.1	5.90
Nahanni (12/23)	1	25.13	0.044	260.94	3.24	17.95	6.41
	2	131.93	0.231	190.563	2.37	7.41	2.65
Northridge	1	30.9	0.082	153.1	2.06	15.43	5.14
	2	7.71	0.020	191.8	2.57	8.73	2.91
	3	15.43	0.041	138.3	1.87	8.95	2.98
	4	3.86	0.010	158.0	2.12	4.40	1.47
	5	17.36	0.046	153.2	2.06	2.93	0.98
Nahanni (10/05)	1	27.84	0.068	228.63	2.65	13.47	4.81
	2	46.40	0.114	250.96	2.90	4.08	1.46
	3	18.56	0.045	159.3	1.84	14.31	5.11
San Fernando (SM)	1	42.86	0.27	240.0	1.60	5.58	1.99
Imperial Valley	1	90.0	0.25	127.0	1.85	16.12	6.20
Superstition Hills #3	1	6.9	0.043	122.7	1.57	7.38	3.07
	2	27.6	0.17	140.5	1.79	12.65	5.27
Morgan Hill	1	3.83	0.013	76.8	4.56	2.80	1.00
	2	3.83	0.013	77.3	4.59	3.72	1.32
	3	3.83	0.013	55.25	3.28	6.00	2.14
	4	3.83	0.013	52.8	3.13	14.0	5.0
	5	23.0	0.077	55.73	3.31	15.40	5.50
	6	3.83	0.013	36.5	2.17	25.63	9.15
North Palm Springs	1	34.2	0.13	36.6	2.10	2.44	0.81
Whittier Narrows	1	4.0	0.04	50.0	1.90	5.02	2.01
	2	9.0	0.09	52.2	1.99	2.69	1.07
	3	2.0	0.02	57.95	2.21	0.71	0.28
	4	2.0	0.02	54.2	2.06	3.04	1.22
Coyote Lake	1	8.0	0.32	114.8	1.51	2.56	0.92

TABLE 4.
Area, Slip, and Hypocentral Distance of Individual Asperities

		Length (km)		Width (km)		Horiz. Dist. (km)		Vert. Dist. (km)	
Earthquake	**Asp#**	**abs**	**norm**	**abs**	**norm**	**abs**	**norm**	**abs**	**norm**
Landers	1	9.0	0.13	7.5	0.5	16.5	0.239	3.75	0.25
	2	12.0	0.174	15.0	1.0	30.0	0.435	7.5	0.5
	3	6.0	0.087	7.5	0.5	48.0	0.696	3.75	0.25
Tabas	1	9.05	0.095	13.5	0.30	4.52	0.0488	6.75	0.15
	2	4.52	0.048	9.0	0.20	2.26	0.0244	31.5	0.70
	3	45.24	0.476	18.0	0.40	36.19	0.381	9.0	0.20
	4	4.52	0.048	13.5	0.30	61.07	0.643	20.25	0.45
	5	4.52	0.048	18.0	0.40	70.12	0.738	9.0	0.20
Loma Prieta	1	8.0	0.200	10.0	0.56	14.0	0.350	11.0	0.61
	2	12.0	0.300	6.0	0.33	26.0	0.650	15.0	0.83
Kobe	1	6.67	0.111	5.0	0.25	3.33	0.056	2.50	0.13
	2	13.33	0.222	20.0	1.00	13.33	0.222	10.0	0.50
Borah Peak	1	19.5	0.40	26.4	1.0	26.0	0.53	13.2	0.50
Nahanni (12/23)	1	10.67	0.308	2.4	0.14	5.33	0.154	1.18	0.07
	2	8.0	0.231	16.49	1.00	14.67	0.423	8.25	0.50
Northridge	1	5.143	0.286	6.0	0.286	2.57	0.143	9.0	0.43
	2	2.57	0.143	3.0	0.143	6.43	0.357	19.5	0.93
	3	5.14	0.286	3.0	0.143	10.29	0.571	10.5	0.50
	4	1.29	0.071	3.0	0.143	10.93	0.607	19.5	0.93
	5	3.86	0.214	4.5	0.214	13.50	0.750	15.75	0.75
Nahanni (10/05)	1	16.00	0.545	1.74	0.13	10.67	0.364	0.87	0.06
	2	5.33	0.182	8.70	0.63	5.33	0.182	9.57	0.69
	3	5.33	0.182	3.48	0.25	18.67	0.636	5.22	0.38
San Fernando (SM)	1	5.34	0.40	8.02	0.67	8.02	0.60	6.68	0.55
Imperial Valley	1	12.0	0.33	7.5	0.75	15.0	0.42	6.25	0.63
Superstition Hills #3	1	3.0	0.15	2.3	0.29	6.5	0.325	2.3	0.29
	2	4.0	0.20	6.9	0.86	14.0	0.70	4.6	0.57
Morgan Hill	1	1.0	0.038	3.83	0.33	0.50	0.019	5.75	0.50
	2	1.0	0.038	3.83	0.33	3.50	0.135	7.67	0.67
	3	2.0	0.077	1.92	0.17	6.0	0.231	8.63	0.75
	4	2.0	0.077	1.92	0.17	14.0	0.538	8.63	0.75
	5	3.0	0.115	7.67	0.67	16.5	0.635	5.75	0.50
	6	2.0	0.077	1.92	0.17	25.0	0.962	2.88	0.25
North Palm Springs	1	6.0	0.30	5.7	0.43	9.0	0.45	8.55	0.64
Whittier Narrows	1	2.0	0.20	2.0	0.20	1.0	0.10	8.0	0.80
	2	3.0	0.30	3.0	0.30	4.5	0.450	7.50	0.75
	3	2.0	0.20	1.0	0.10	5.0	0.500	4.50	0.45
	4	2.0	0.20	1.0	0.10	8.0	0.800	4.50	0.45
Coyote Lake	1	3.0	0.55	2.67	0.58	2.5	0.45	2.1	0.46

TABLE 5.
Dimensions and Locations of Individual Asperities
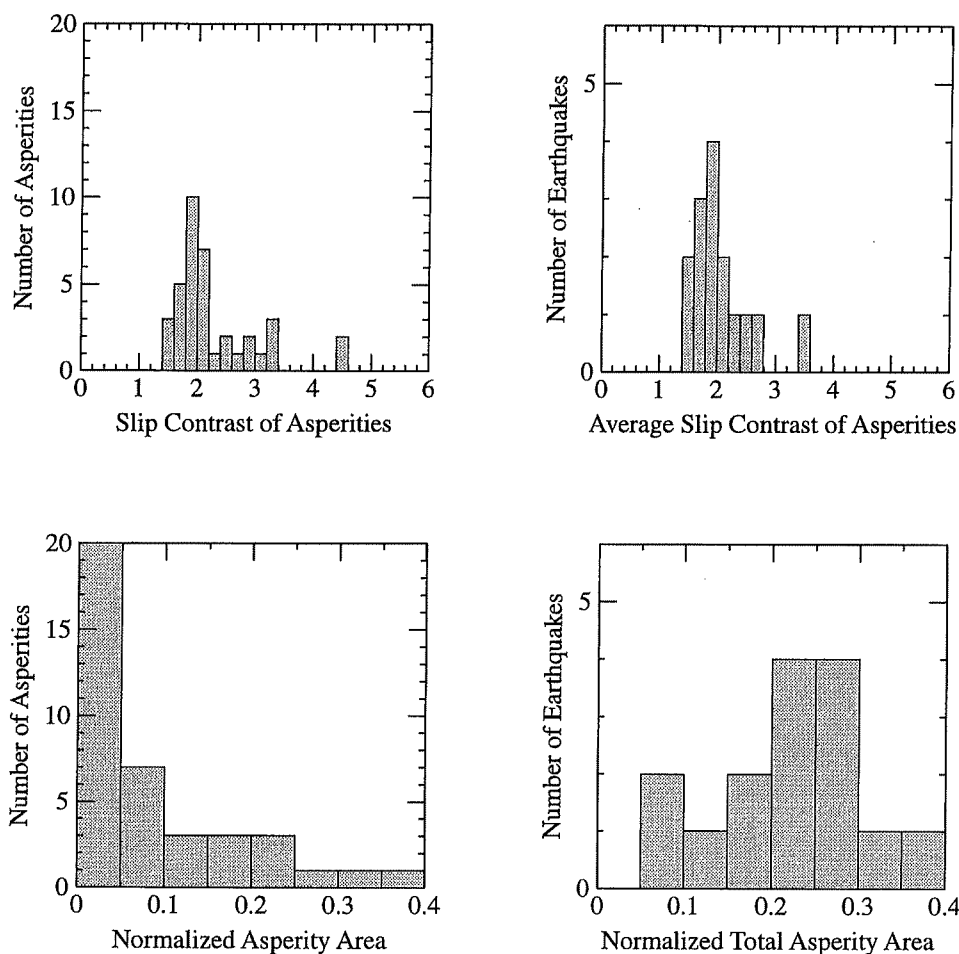
▲ Figure 3. Upper left: Distribution of values of average slip of individual asperities normalized to the average slip of the overall rupture. Lower left: Distribution of values of individual asperity slip area normalized to the overall rupture area. Upper right: Distribution of values of average asperity slip for each earthquake, normalized to the average slip of the overall rupture. Lower right: Distribution of values of combined asperity slip area for each earthquake, normalized to the overall rupture area.

In all, the fifteen earthquakes have thirty-nine asperities, or 2.6 asperities each on average. In Figure 3, we plot histograms of the distribution of slip contrast (the average slip on the asperities as a fraction of the average slip of the overall rupture) and normalized asperity area (the area of the asperity as a fraction of the fault rupture area) in this set of thirty-nine asperities. The slip contrast has an asymmetrical distribution, with most asperities having a ratio between 1.5 and 3.0. The cutoff at 1.5 is due to the definition of an asperity as a region whose slip is larger than 1.5 times the average slip. Individual asperities typically occupy a few percent of the rupture area, with the largest asperity on average occupying 17.5% of the overall rupture area.

In addition to analysis of the properties of individual asperities, we analyze the overall average properties of asperities for each earthquake. In Table 6 we list for each event the number of asperities, the total fault rupture area, the overall area of the asperities, their overall area as a fraction of the total rupture area, the average fault slip, the maximum fault

slip, the average slip on the asperities, and the slip contrast. In Figure 3, we also plot histograms of the distribution of slip contrast and normalized asperity area values, each value representing the average over the asperities for a single earthquake. The slip ratio is concentrated in the range of 1.5 to 2.8, with an average value of about 2. Asperities make up about 22% of the total rupture area on average and account for 44% (that is, 2 times 22%) of the total slip on the fault.
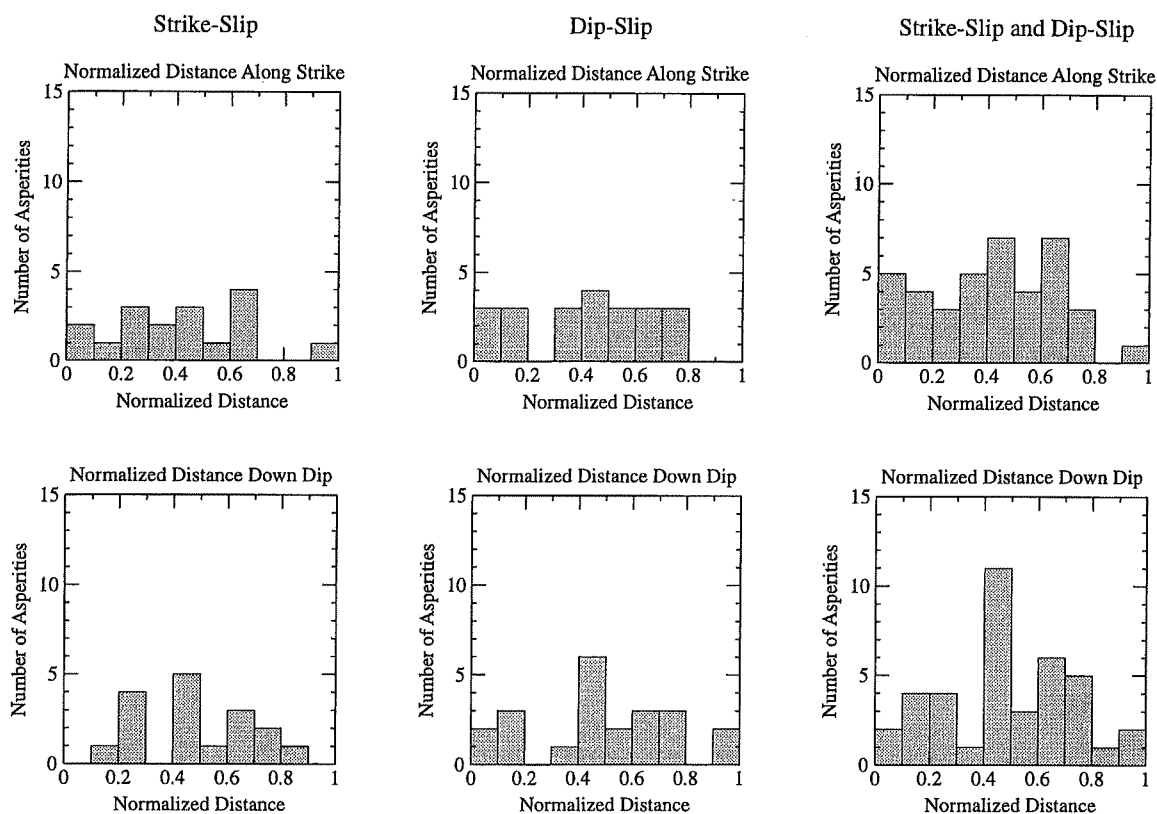
Asperities on both strike-slip and dip-slip faults tend to have along-strike length to down-dip width ratios (aspect ratios) of about 1, except for the two Nahanni events, which each have a long, narrow asperity at the top of the fault rupture. In contrast, the mainshock rupture zones of the seven strike-slip faults (including the oblique Loma Prieta earthquake) have an average aspect ratio of 2.75, whereas the those of the eight dip-slip faults (including the oblique North Palm Springs event) have an average aspect ratio of 1.6. These findings are reflected in the statistics of the dimensions of individual asperities shown in Figure 4. The distributions of

TABLE 6.
Asperity Parameters of Individual Earthquakes

Earthquake	Area (km²)	Av. Slip (cm)	Max. Slip (cm)	Asperity Area (km²)	Asperity Area Norm./Area	Av. Asp. Slip (cm)	Av. Asp. Slip Norm./Av Slip
Landers	1035	269	794	293	0.28	305	1.84
Tabas	4275	50	213	1120	0.26	116	2.33
Loma Prieta	720	166	496	152	0.10	290	1.75
Kobe	1200	67	348	300	0.25	125	1.88
Borah Peak	1287	47	147	515	0.40	75.6	1.62
Nahanni (12/23)	572	80	516	157	0.27	202	2.51
Northridge	378	74	286	75	0.20	154	2.07
Nahanni (10/05)	408	86	383	93	0.23	226	2.62
San Fernando (SM)	161	150	300	43	0.27	240	1.60
Imperial Valley	360	69	180	90	0.25	127	1.85
Superstition Hills 3	161	78	186	35	0.21	137	1.75
Morgan Hill	299	17	100	42	0.14	57.6	3.42
North Palm Springs	266	17	45	34	0.13	36.5	2.10
Whittier Narrows	100	26	90	17	0.17	52.6	2.00
Coyote Lake	25	76	120	8	0.35	115	1.51
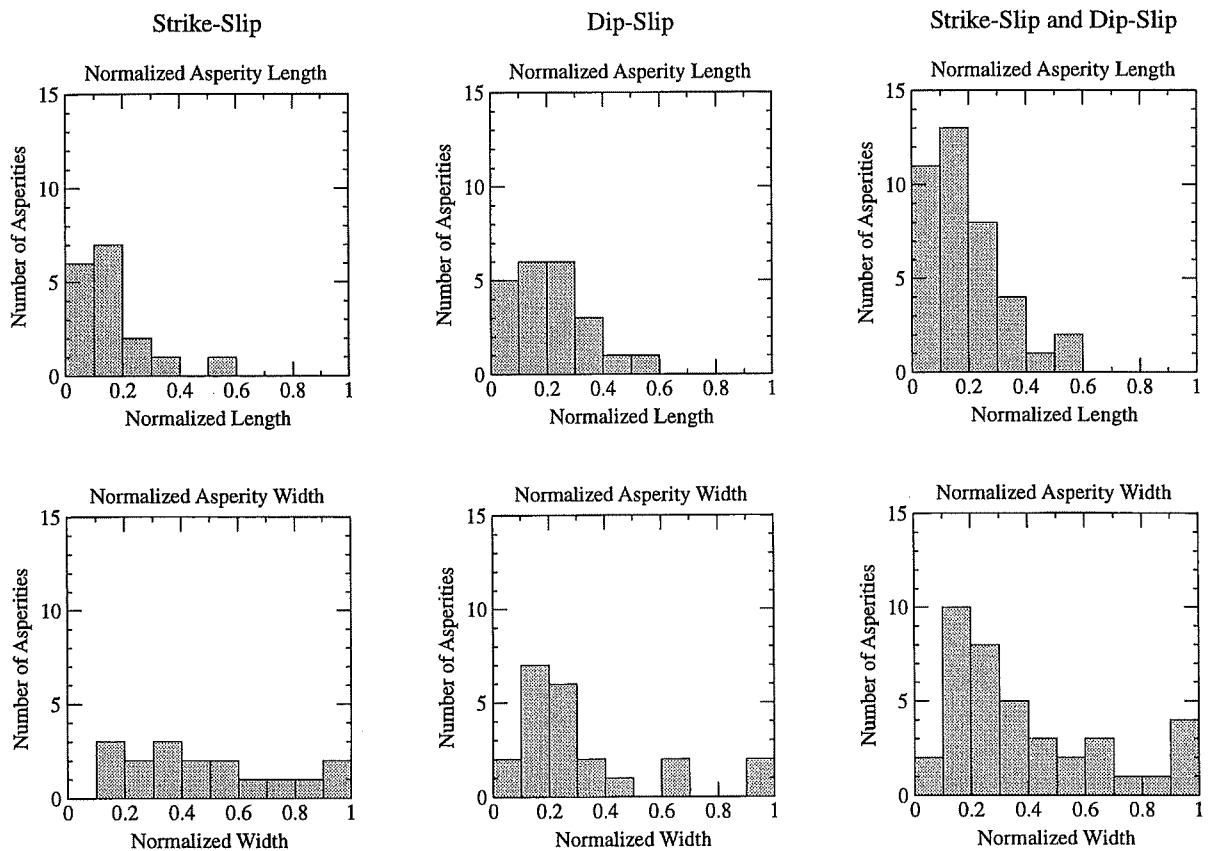
▲ **Figure 4.** Distributions of asperity length and width, normalized to the length and width of the fault rupture, for strike-slip, dip-slip, and all events.

Strike-Slip   Dip-Slip   Strike-Slip and Dip-Slip

▲ Figure 5. Distributions of locations of the centers of asperities along-strike and down-dip, normalized to the length and width of the fault rupture, for strike-slip, dip-slip, and all events.

asperity length and width, normalized to the length and width of the fault rupture, are similar for the dip-slip events. However, the distributions of normalized asperity length and width are different for the strike-slip events, having much lower normalized lengths than normalized widths.

The centers of asperities of both strike-slip and dip-slip faults are distributed fairly evenly both along strike and down-dip, as shown in Figure 5. The down-dip distribution for both styles of faulting tends to have a trimodal distribution, with asperities concentrating at depths of 0.2, 0.45, and 0.7 times the down-dip width.

SCALING OF PARAMETERS OF SLIP MODELS WITH SEISMIC MOMENT

We can use the large range of seismic moment values of the fifteen earthquakes listed in Table 1 to look for systematic features of the scaling of slip models with magnitude. These scaling relations, listed in Table 7, are important for establishing general rules for developing source models for simulating strong ground motions. The simplest scaling relationship is a self-similar one in which the basic properties of the slip models, and of the asperities that they contain, remain scale invariant. The basic property of a self-similar system is that events of different sizes cannot be distinguished except by a scale factor.

The relationship between seismic moment and fault parameters is given by:

$$M_o = \mu D\,L\,W$$

where M_o is seismic moment, μ is shear modulus, D is average fault displacement, L is fault length, and W is fault width. In a self-similar system, increase in seismic moment occurs by proportionately equal changes in average slip D, fault length L, and fault width W so that the stress drop (proportional to the ratio of D to L or W) remains constant. Also, the duration of slip on the fault T_R increases in proportion to D, or equivalently to L or W, so that the slip velocity (the ratio of D to T_R) remains constant. In this self-similar model, the size of asperities in relation to L (and W) remains constant, their average slip in relation to D (slip contrast) remains constant, and the number of asperities remains constant.

The self-similar model is convenient to use, and in many instances its use can be justified because it provides a reasonably good description of nature. For example, Tanioka and Ruff (1997) found that the teleseismic source time functions of large earthquakes are compatible with a self-similar scaling model. In this study of crustal earthquakes, we find that the scaling of the fault parameters described above with seismic moment is also reasonably well fit by a self-similar model. For each parameter, we first give the unconstrained scaling relation and then the relation that is constrained to be self-similar. The

TABLE 7. Scaling Relations of Slip Models Assuming Self-Similarity	
Rupture Area vs. Seismic Moment	$A = 2.23 \times 10^{-15} \times M_0^{2/3}$
Average Slip vs. Seismic Moment	$D = 1.56 \times 10^{-7} \times M_0^{1/3}$
Combined Area of Asperities vs. Seismic Moment	$A_a = 5.00 \times 10^{-16} \times M_0^{2/3}$
Area of Largest Asperity vs. Seismic Moment	$A_l (\text{km}^2) = 3.64 \times 10^{-16} \times M_0^{2/3}$
Radius of Largest Asperity vs. Seismic Moment	$r_l (\text{km}) = 1.08 \times 10^{-8} \times M_0^{1/3}$
Average Number of Asperities	2.6
Area of Fault Covered by Asperities	0.22
Average Asperity Slip Contrast	2.01
Hypocentral Distance to Center of Closest Asperity vs. Moment	$R_A = 1.35 \times 10^{-8} \times Mo^{1/3}$
Slip Duration vs. Seismic Moment	$T_R = 2.03 \times 10^{-9} \times Mo^{1/3}$
Corner Spatial Wavenumber Along Strike (km^{-1})	$\log KC_x = 1.72 - 0.5\ M$
Corner Spatial Wavenumber Down Dip (km^{-1})	$\log KC_y = 1.93 - 0.5\ M$

difference between these two relations provides an indication of how closely the data satisfy the self-similar scaling relation. For each relationship, the scatter in the data is sufficiently large that the self-similar scaling relation is compatible with the data. We expect that limits in the dimensions of faults (especially the down-dip width W) are reached for very large crustal earthquakes, especially strike-slip earthquakes, causing departures from this self-similar model (Shimazaki, 1986). However, for the moderate-sized crustal earthquakes that make up most of the data set that we analyze here, we conclude that the self-similar model is a reasonable approximation. Except where noted, all of the relationships use cgs units.

Rupture Area vs. Seismic Moment

The relation between rupture area A and seismic moment M_o determined without constraining the slope is:

$$A = 1.30 \times 10^{-18} \times M_o^{0.79}$$

Constraining the slope to be 2/3, we obtain the relation shown in Figure 6:

$$A = 2.23 \times 10^{-15} \times M_o^{2/3}$$

Expressing this relation in terms of moment magnitude M and area in square km, we obtain:

$$M = \log A + 3.95$$

where moment magnitude M (Hanks and Kanamori, 1979) is given by:

$$M = 2/3 \log M_o - 10.7$$

The fault rupture areas used in this relation reflect the zone of the fault that radiated seismic energy, and so this relation is directly relevant to the prediction of strong ground motion. Wells and Coppersmith (1994) derived a relationship between seismic moment and rupture area from a much larger set of crustal earthquakes, primarily using the dimensions of the early aftershock zone. This is a less direct kind of evidence than that derived from the seismic radiation during the mainshock. Nevertheless, the Wells and Coppersmith (1994) relationship for a dataset that includes all styles of faulting is very similar to the one derived here and is given by:

$$M = 0.98 \log A + 4.07$$

Average Slip vs. Seismic Moment

The relation between average slip D and seismic moment M_o determined without constraining the slope is:

$$D = 3.16 \times 10^{-7} \times M_o^{0.32}$$

Constraining the slope to be 1/3, we obtain the self-similar relation shown in Figure 7:
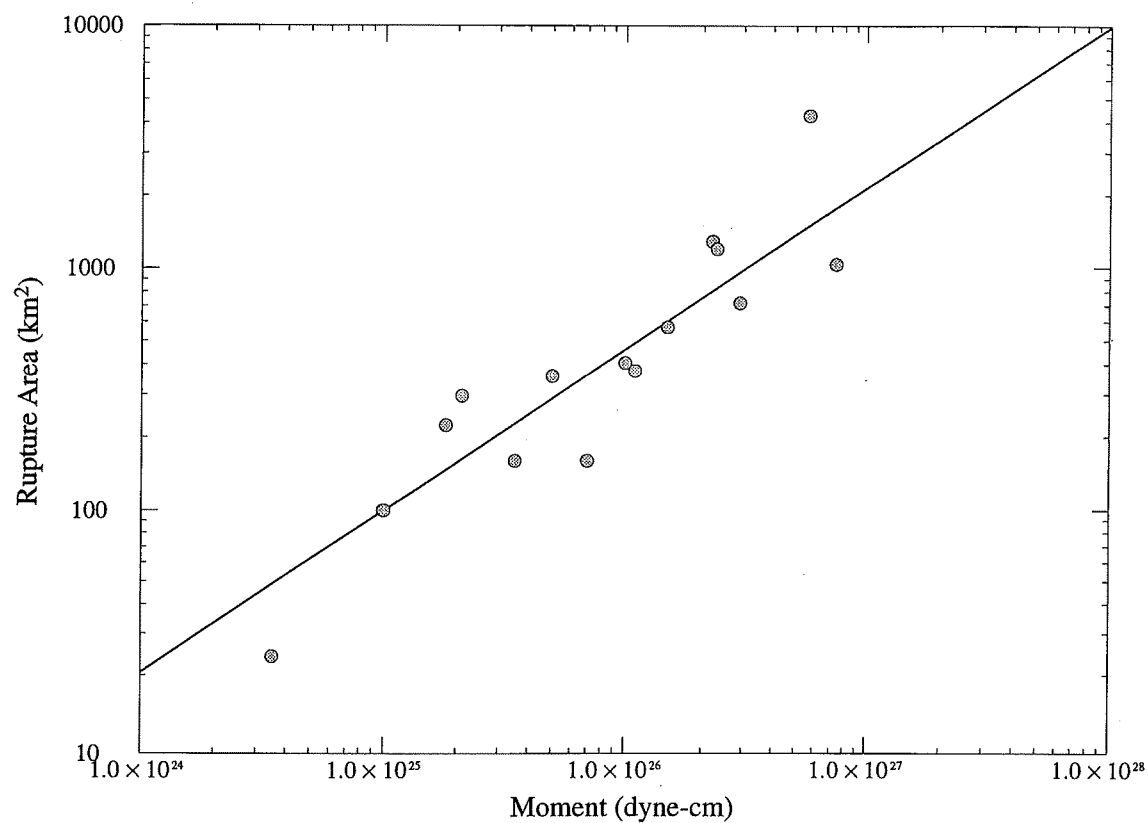
$$D = 1.56 \times 10^{-7} \times M_o^{1/3}$$

Combined Area of Asperities vs. Seismic Moment

The relation between the combined area of asperities A_a and seismic moment M_o determined without constraining the slope is:
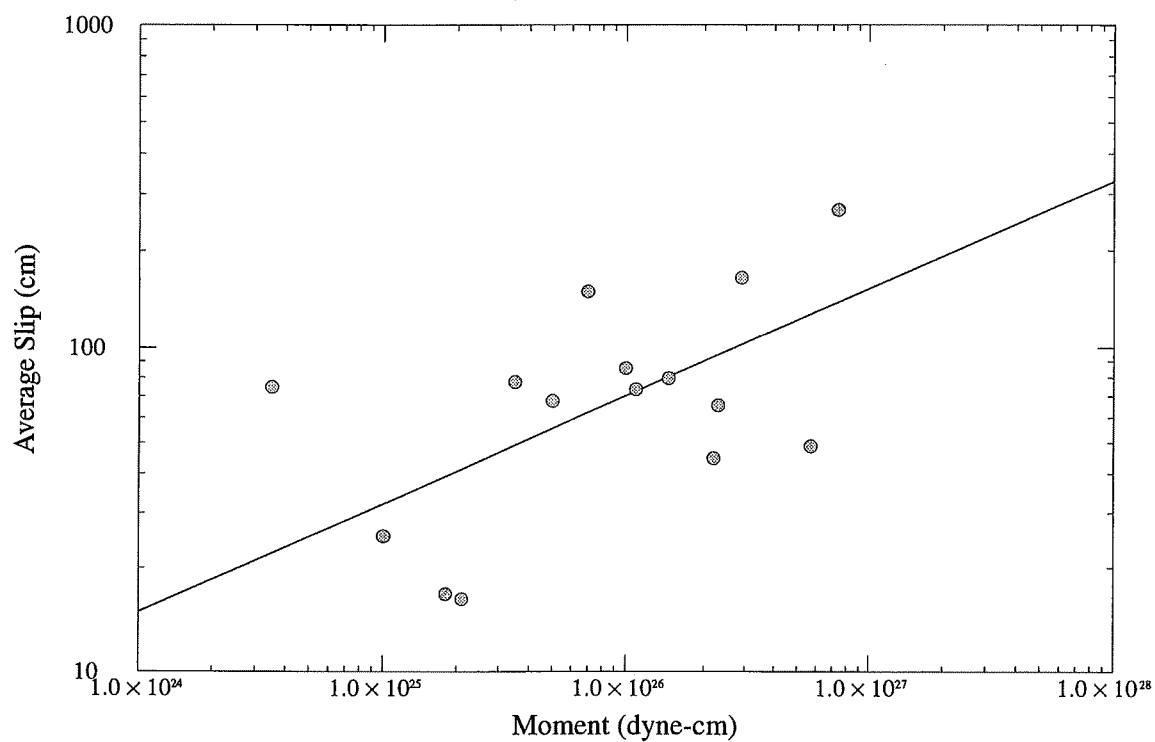
$$A_a = 5.93 \times 10^{-21} \times M_o^{0.86}$$

Constraining the slope to be 2/3, we obtain the self-similar relation shown in Figure 8:
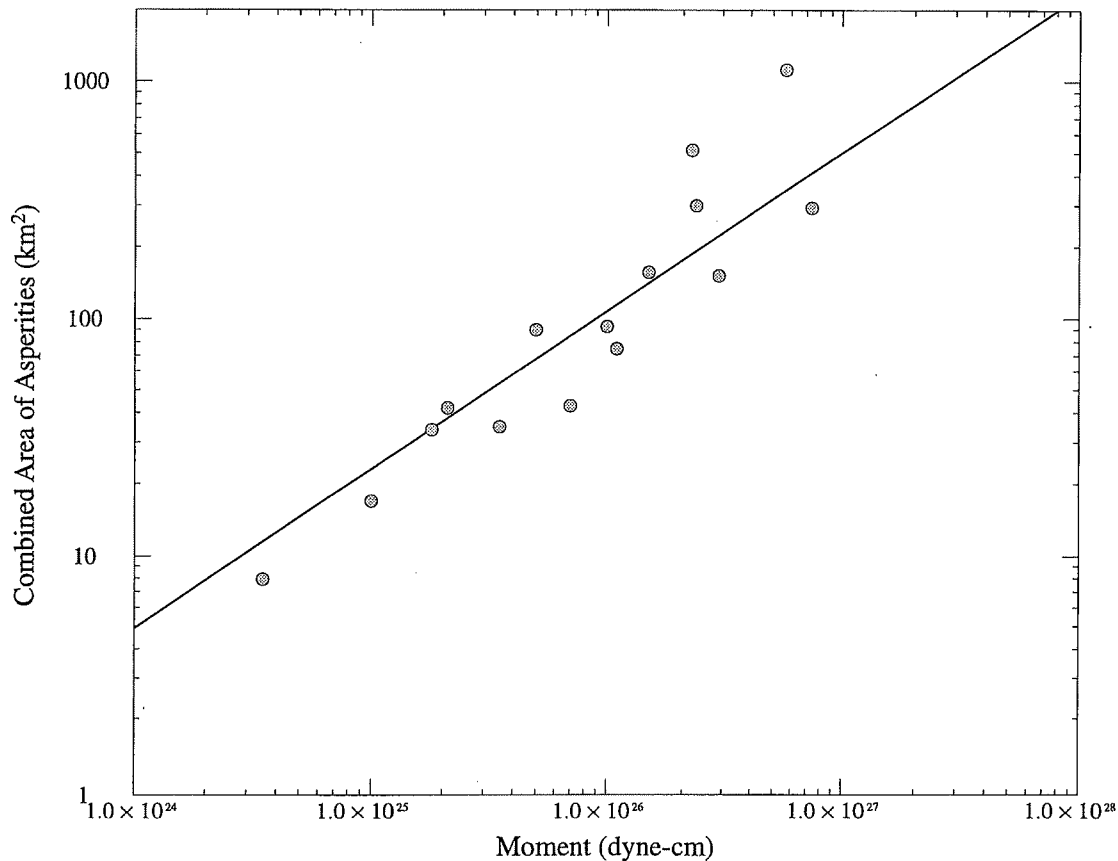
$$A_a = 5.00 \times 10^{-16} \times M_o^{2/3}$$

▲ **Figure 6.** Relation between rupture area and seismic moment. Dots represent individual events, and the line is a least-squares fit under the constraint of self-similarity (slope = 2/3).

▲ **Figure 7.** Relation between average slip and seismic moment. Dots represent individual events, and the line is a least-squares fit under the constraint of self-similarity (slope = 2/3).

▲ Figure 8. Relation between combined area of asperities and seismic moment. Dots represent individual events, and the line is a least-squares fit under the constraint of self-similarity (slope = 2/3).

The ratio of the combined area of asperities to the total rupture area shows no clear dependence on seismic moment, and its value averaged over these events is 22%. The two events in which asperities cover a large part of the fault are the Borah Peak and Coyote Lake events. The four events in which asperities cover a small part of the fault are the Loma Prieta, North Palm Springs, Morgan Hill, and Whittier Narrows earthquakes.

Area of Largest Asperity vs. Seismic Moment

The relation between the area of the largest asperity A_l and seismic moment M_o determined without constraining the slope is:

$$A_l = 1.74 \times 10^{-21} \times M_o^{0.87}$$

Constraining the slope to be 2/3, we obtain the self-similar relation shown in Figure 9:

$$A_l \, (\text{km}^2) = 3.64 \times 10^{-16} \times M_o^{2/3} \, (\text{dyne-cm}) \text{ or}$$

$$r_l \, (\text{km}) = 1.08 \times 10^{-8} \times M_o^{1/3} \, (\text{dyne-cm})$$

where r_l is the radius of a circular asperity. The area of the largest asperity in each slip model scales in an approximately self-similar way and on average occupies 17.5% of the total rupture area. The radius r_a of the average asperity is:

$$r_a \, (\text{km}) = 0.78 \times 10^{-8} \times M_o^{1/3} \, (\text{dyne-cm})$$

## Average Asperity Slip Contrast vs. Seismic Moment

The average asperity slip contrast shows no clear dependence on seismic moment, consistent with a self-similar scaling relation, and its value averaged over these events is 2.01. Events having the largest slip contrasts are the Morgan Hill event, the two Nahanni events, and the Tabas event.

Hypocentral Distance to Closest Asperity vs. Seismic Moment

The question of whether earthquake ruptures begin at asperities is potentially important both for rupture dynamics and for strong-motion prediction. The distances between the hypocenter and the centers of individual asperities are listed in Table 4, and the relation between the hypocentral distance to the center of the closest asperity R_A and the seismic moment M_o is shown in Figure 10. The relation determined without constraining the slope is:
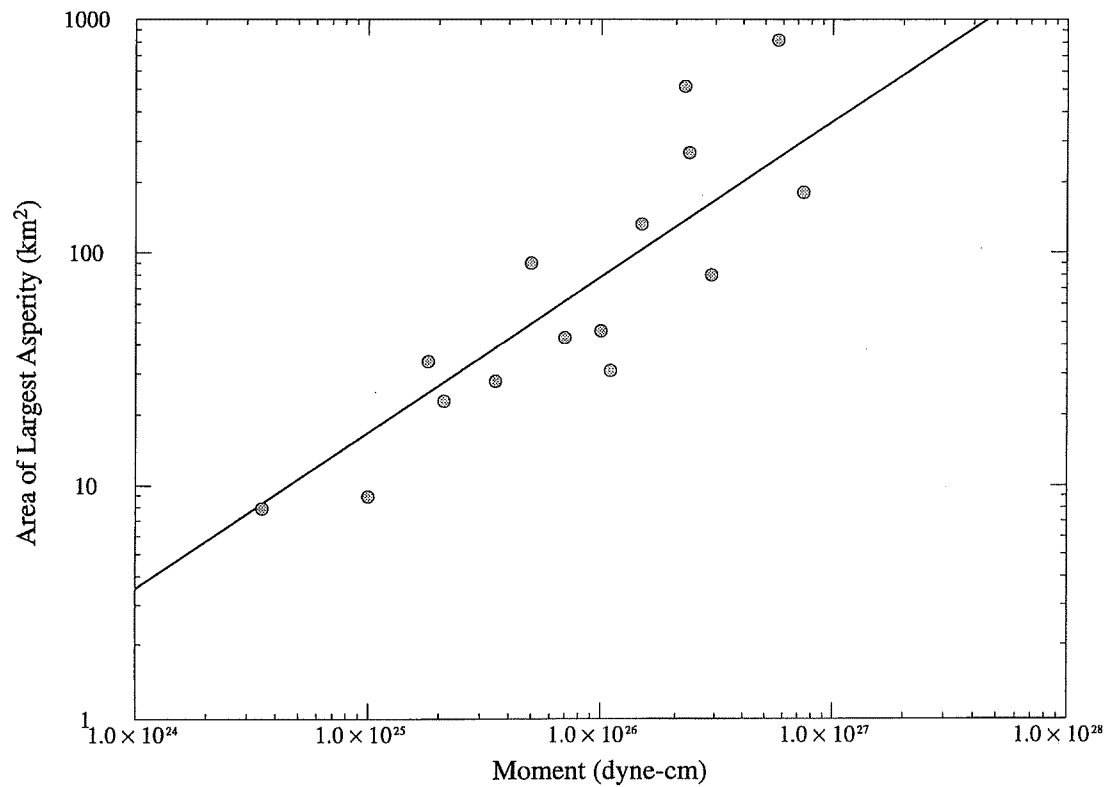
▲ **Figure 9.** Relation between area of largest asperity and seismic moment. Dots represent individual events, and the line is a least-squares fit under the constraint of self-similarity (slope = 2/3).
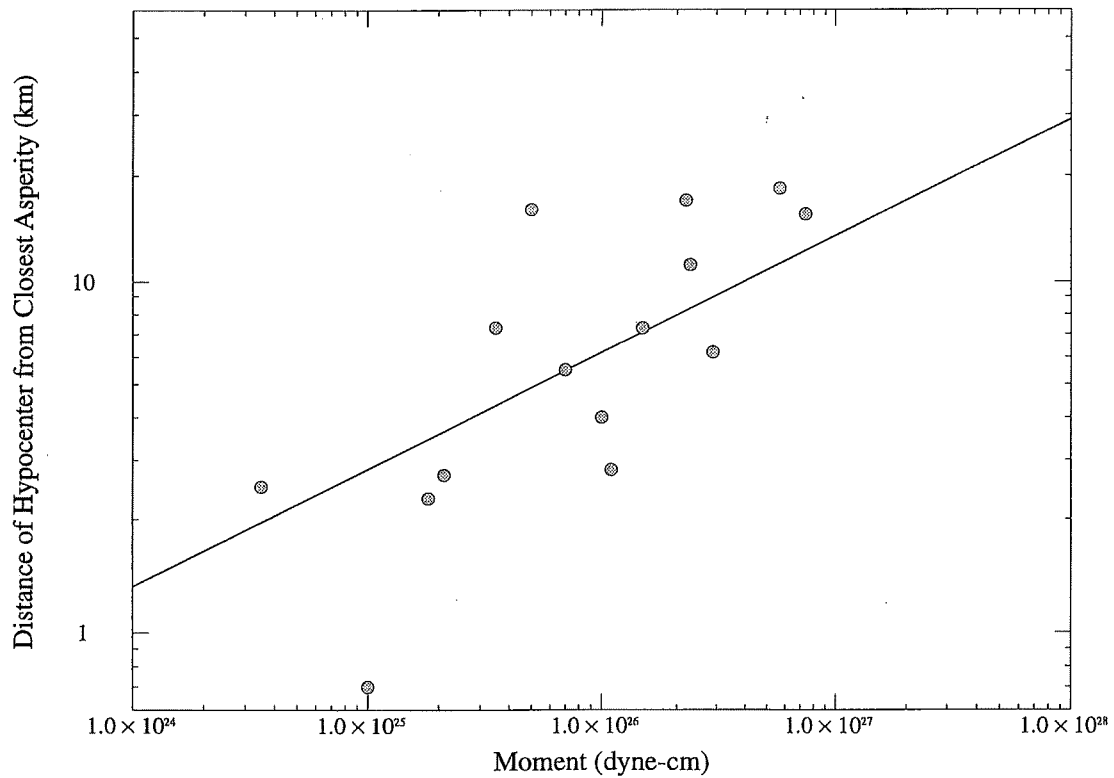
▲ **Figure 10.** Relation between distance from the hypocenter to the center of the closest asperity and seismic moment. Dots represent individual events, and the line is a least-squares fit under the constraint of self-similarity (slope = 1/3).

$$R_A = 1.43 \times 10^{-13} \times M_o^{0.53}$$

If the hypocenter were located at the center of an asperity, then the distance between the hypocenter and the center of the closest asperity would not increase with seismic moment. The fact that this distance does increase with seismic moment indicates that the location of the hypocenter is not correlated with the location of the closest asperity. The unconstrained relationship indicates that the distance between the hypocenter and the closest asperity, normalized to the fault dimension, increases with seismic moment. Constraining the slope of the relation to be 1/3, which represents the case where the normalized distance is invariant with seismic moment, we obtain the self-similar relation shown in Figure 10:

$$R_A = 1.35 \times 10^{-8} \times M_o^{1/3}$$

This distance is 1.7 times larger than the radius r_a of the average asperity, indicating that on average the hypocenter is located outside of the closest asperity.

Hypocentral Distance to Largest Asperity vs. Seismic Moment

Of the ten events with more than one asperity, which on average have 3.4 asperities, three have hypocenters closest to the largest asperity and seven have hypocenters closest to other asperities. This indicates that the hypocenter is not systematically located closest to the largest asperity. The relation between the hypocentral distance to the center of the largest

asperity R_l and seismic moment M_o, determined without constraining the slope, is:

$$R_l = 2.63 \times 10^{-12} \times M_o^{0.45}$$

Constraining the slope of the relation to be 1/3, which represents the case where the distance, normalized to fault dimension, is invariant with seismic moment, we obtain the self-similar relation:

$$R_l = 2.09 \times 10^{-8} \times M_o^{1/3}$$
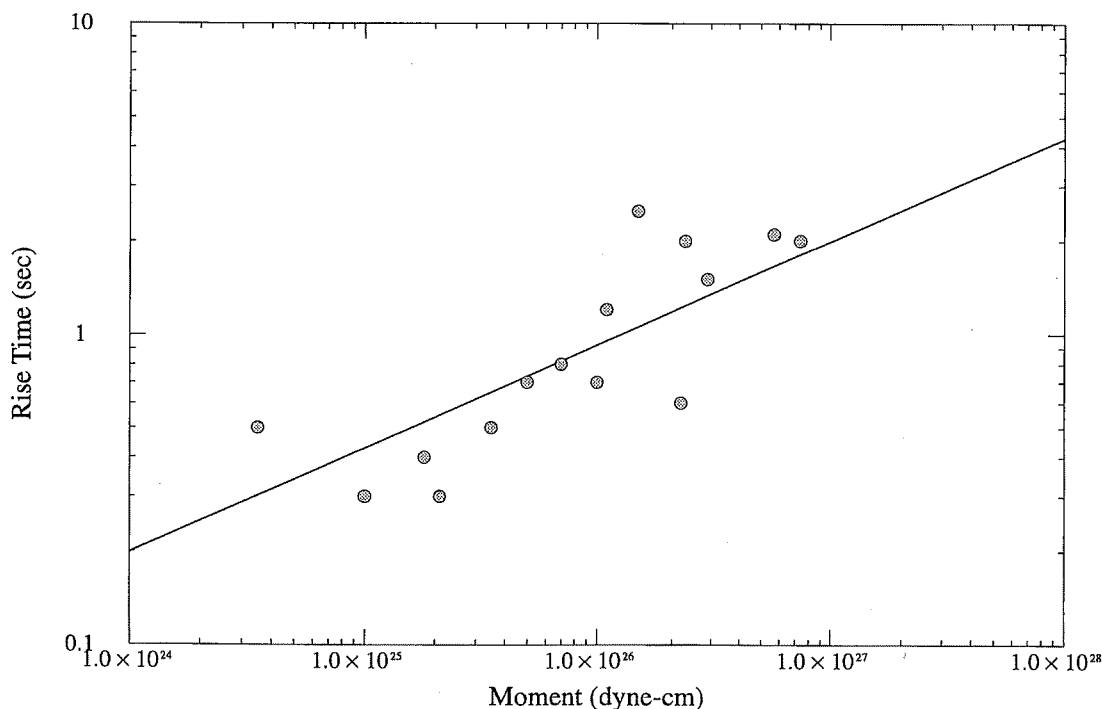
Slip Duration vs. Seismic Moment

The slip duration listed in Table 1 is chosen to represent an average over the fault surface for a given earthquake. The relation between slip duration and seismic moment determined without constraining the slope is:

$$T_R = 1.48 \times 10^{-11} \times M_o^{0.42}$$

Constraining the slope to be 1/3, we obtain the self-similar relation shown in Figure 11:

$$T_R = 2.03 \times 10^{-9} \times M_o^{1/3}$$

This rise time is similar to the rupture duration of the largest asperity, using the above relation between seismic moment and dominant asperity dimension and assuming a rupture velocity of 2.7 km/sec.

▲ **Figure 11.** Relation between slip duration and seismic moment. Dots represent individual events, and the line is a least-squares fit under the constraint of self-similarity (slope = 1/3).

Rupture Velocity

The rupture velocities V_R of the slip models, listed in Table 1, fall within the fairly narrow range of 2.4 to 3.0 km/sec, with an average value of 2.73, and there is no evidence of a dependence of rupture velocity on seismic moment.

WAVENUMBER SPECTRUM ANALYSIS OF SPATIAL HETEROGENEITY IN SLIP

In the above analysis, we have made some approximate quantitative estimates of the parameters of slip models and analyzed their scaling with seismic moment. In this section, we follow an alternative approach to quantifying slip models for use in developing characteristic slip models of future earthquakes. To characterize the spatial variation in slip in a way that is useful for constructing slip models, we have analyzed the 2-D Fourier transforms of the slip functions summarized above. In taking the Fourier transform, we are viewing the slip function as the sum of a series of slip functions each of which is a 2-D sinusoidal function having a single spatial wavelength. The two dimensions are the dimension along-strike and the dimension down-dip. The Fourier transform describes the relative amplitudes of these different spatial wavelengths in the slip model.

It is conventional to describe the spatial wavelength in terms of its reciprocal, the spatial wavenumber. Small wavenumbers are equivalent to long wavelengths and represent broad fluctuations of slip over the fault surface, while large wavenumbers are equivalent to short wavelengths and represent local fluctuations over the fault surface. The spatial sampling of the fault in the along-strike and down-dip directions controls the highest wavenumber (Nyquist frequency) for which the slip model is complete. These maximum spatial wavenumbers are listed in Table 3. To eliminate poorly sampled information at higher wavenumbers, we lowpass filtered the wavenumber spectra using a cosine filter that was unity at the Nyquist frequency and zero at twice the Nyquist frequency. We did not consider it necessary to filter the slip models at lower wavenumber, because the slip models are generated using a distribution of point sources covering each fault element, and so they are effectively derived from a sampling that is more dense than the Nyquist. All of the slip models were resampled at 1 km spacing using bilinear interpolation. The slip distributions were also padded with zeros to 128 km in each direction. This produced even sampling of the wavenumber spectra.

As an example, we show the spatial wavenumber spectra of the 1989 Loma Prieta earthquake in Figure 12. k_x is the wavenumber along-strike and k_y is the wavenumber down-dip. We show only the amplitude spectrum, which describes the relative amplitudes of the different wavenumbers that compose the spectrum. The phase spectrum determines the way in which these components are summed to produce the particular pattern of slip by constructive and destructive

interference. There is an infinite number of slip models that satisfy a single wavenumber amplitude spectrum.

The gradient of the contours represents the rate at which the amplitude of slip decreases with decreasing wavelength or increasing wavenumber. A steep gradient indicates a relatively smooth spatial variation in slip, while a gradual gradient indicates a relatively abrupt spatial variation in slip. As described above, the asperities of strike-slip and dip-slip faults both tend to have aspect ratios of about 1. Generally, the strike-slip and oblique-slip earthquakes have a more rapid decay of wavenumber in the along-strike direction than in the down-dip direction, indicating more rapid variation in slip down-dip than along-strike, relative to the dimensions of the fault. In contrast, the wavenumber spectra of dip-slip faults have more similar decay of wavenumber along-strike and down-dip.

We obtained the parameters of a wavenumber spectral model of the slip distribution in earthquakes by fitting a simple functional form to the wavenumber spectra of individual earthquakes. We used 2-D Butterworth filters to model the wavenumber amplitude spectrum.

The corner wavenumbers KC_x and KC_y in the along-strike and down-dip directions respectively were assumed each to have a self-similar scaling with moment magnitude M. For self-similar scaling, the corner wavenumber is inversely proportional to the one-third power of seismic moment, and the logarithm of the corner wavenumber is proportional to one half the moment magnitude. The least squares fit resulted in the following model:

$$\log KC_x = 1.72 - 0.5\ M$$

$$\log KC_y = 1.93 - 0.5\ M$$

The Butterworth filters have 2.0 poles, and the corner wavenumbers are approximately log normally distributed with a standard error of 0.26. The wavenumber amplitude is given by:

$$\mathrm{amp}(kx,ky) = \frac{1}{\sqrt{\left(1 + \left(\left(\frac{kx}{KC_x}\right)^2 + \left(\frac{ky}{KC_y}\right)^2\right)^{2.0}\right)}}$$

This spectrum falls off as the inverse of the wavenumber squared at high wavenumbers, consistent with the model of Herrero and Bernard (1994). In Figure 13, we compare a simplified form of our normalized model where KC is approximated by the inverse of the fault dimension L:

$$\mathrm{amp}(k) = [1 + (kL)^4]^{-\frac{1}{2}}$$

with the model of Herrero and Bernard (1994):

Loma Prieta

taper corners: $kx = 0.25$ $ky = 0.25$

Amplitude (log10)
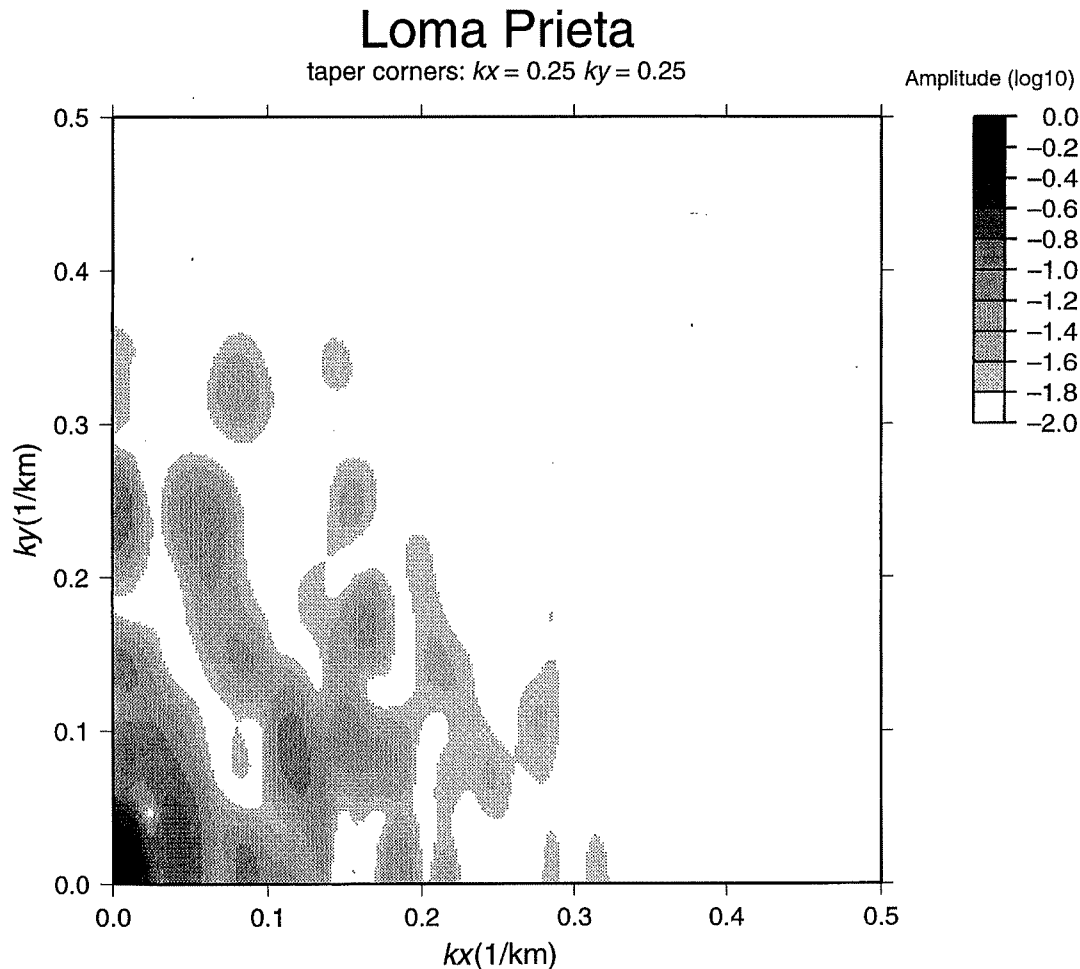
▲ **Figure 12.** Spatial wavenumber spectrum of the 1989 Loma Prieta, California earthquake.

$$\text{amp}(k) = \begin{cases} 1, & k < 1/L \\ \left(\dfrac{1}{kL}\right)^2, & k > 1/L \end{cases}$$

Figure 13 demonstrates that these two models have the same decay at high wavenumber. Herrero and Bernard (1994) based their model on the assumption of self-similarity in slip distribution, independent of seismic moment. They showed that this is consistent with the stochastic fault model of Andrews (1981), which has a stress drop that decays as the inverse of the wavenumber. The model of Herrero and Bernard (1994) is also consistent with the fractal model of Frankel (1991) when the fractal dimension is 2.

Herrero and Bernard (1994) show that the wavenumber-squared model, when combined with the assumptions of constant rupture velocity and scale-dependent rise time, results in a kinematic source model whose frequency spectrum falls off as the inverse of the frequency squared. This frequency squared decay was first proposed by Aki (1967) and is commonly found to describe the source spectra of earthquakes (e.g., Houston and Kanamori, 1986). As pointed

out by Herrero and Bernard (1994), the assumption of constant rupture velocity is probably too restrictive. They consider that the wavenumber spectrum may actually include the effects of spatial variations in slip distribution, rupture velocity, and slip velocity, which combine to give a decay with wavenumber that is approximately a power of two.

In Figure 14, we compare the fit of our model to four earthquakes which span the range of magnitudes in our data set and which have some of the largest values of maximum spatial wavenumber. As described above and listed in Table 3, the spatial sampling of the fault in the along-strike and down-dip directions controls the maximum wavenumber for which the slip model is complete. Figure 14 indicates that our empirical model of the wavenumber spectrum is not well constrained for wavenumbers higher than about 0.4 km^{-1}. However, at high wavenumbers our empirical model has exactly the same decay as the theoretical model of Herrero and Bernard (1994). This suggests that our wavenumber model may be reliable for higher wavenumbers and that, given our current state of knowledge, it is reasonable to use our empirical wavenumber model to generate slip models for the prediction of high-frequency ground motion.
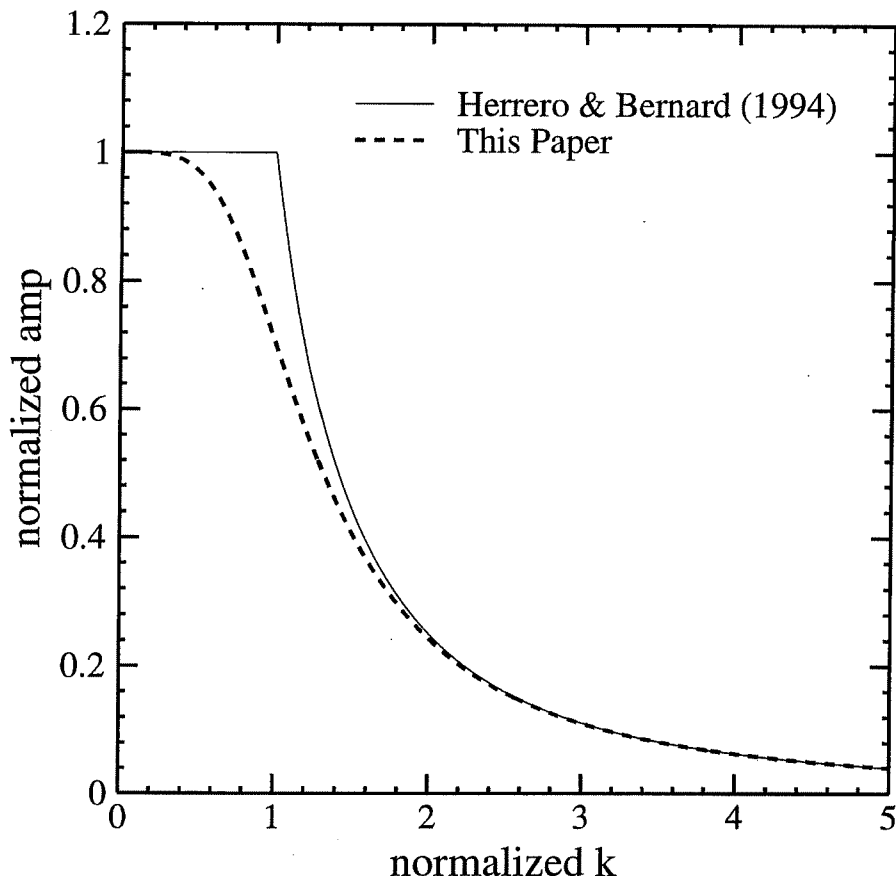
▲ Figure 13. Comparison of a simplified version of our wavenumber spectral model with that of Herrero and Bernard (1994).

SUMMARY

Over the past fifteen years, slip models have been derived for enough crustal earthquakes that we can now identify systematic features of these slip models and their scaling with seismic moment for use in the prediction of strong ground motion. We have used two approaches in our analysis of these slip models. The first approach is to use a set of parameters to quantify in a deterministic manner the properties of slip models and asperities. The second approach is to quantify the heterogeneity of slip on the fault surface by its two-dimensional Fourier transform (the wavenumber spectrum). In developing a method of generating slip models of future earthquakes, we can use the asperity characteristics derived from the first approach to constrain a model of the wavenumber spectrum based on the second approach.

In characterizing the slip models, we first analyzed the depth distribution of slip. For strike-slip and oblique faults, slip tends to increase with depth toward the central or lower region of the rupture plane. For dip-slip faults, the distribution of slip with depth is less systematic, and it is possible that slip is concentrated at shallower depths. We defined an asperity as a region in which the slip is larger by a prescribed amount than the average slip over the fault surface. We found that slip models and the asperities on them scale in a

self-similar manner with increasing seismic moment. In this self-similar system, increase in seismic moment occurs by proportionately equal changes in average slip D, fault length L, and fault width W so that the stress drop (proportional to the ratio of D to L or W) remains constant. Also, the duration of slip on the fault T_R increases in proportion to D, or equivalently to L or W, so that the slip velocity (the ratio of D to T_R) remains constant. The size of asperities in relation to L (and W) remains constant, their average slip in relation to D (slip ratio) remains constant, and the number of asperities remains constant.

Some quantitative measures of these self-similar scaling relationships are as follows. The combined area of asperities scales in a self-similar way with increasing seismic moment, being proportional to the two-thirds power of seismic moment. The combined area of asperities on average occupies 22% of the total rupture area. The area of the largest asperity in each slip model also scales in an approximately self-similar way, and on average occupies 17.5% of the total rupture area. The slip contrast of asperities (the ratio of average slip on asperities to average slip over the whole rupture surface) is independent of seismic moment, consistent with the self-similar scaling law, and its average value for the events studied is about 2. There is no correlation between the location of the hypocenter and the locations of the closest or
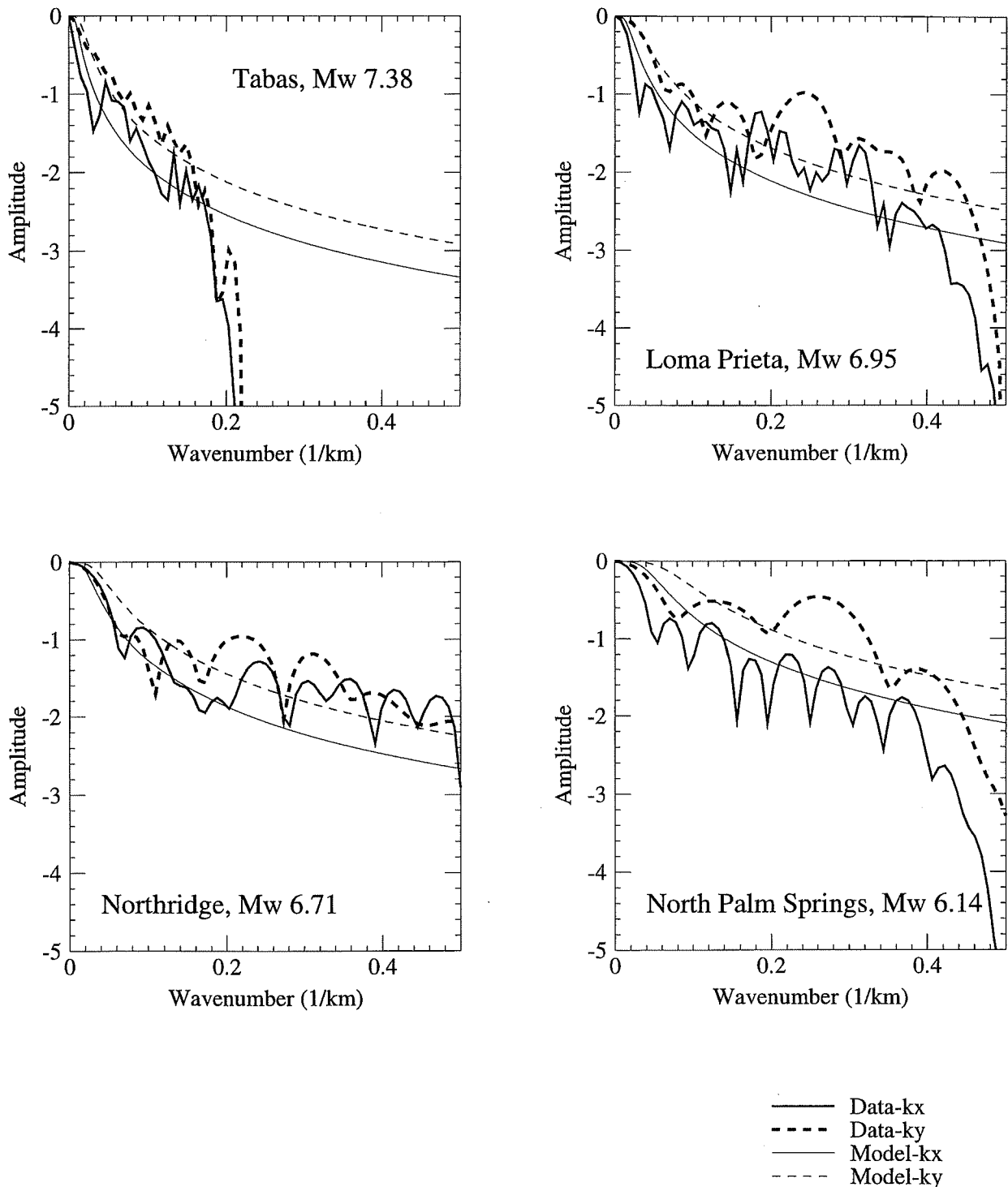
▲ Figure 14. Comparison of our spectral wavenumber model with the wavenumber spectra of four earthquakes that span the magnitude range of our dataset.

largest asperities, and the hypocenter usually lies outside the closest asperity. On average, the slip duration scales in a self-similar way with seismic moment, being proportional to the one-third power of seismic moment. The rupture velocities of the slip models fall within the fairly narrow range of 2.4 to 3.0 km/sec and show no dependence on seismic moment.

An alternative method of representing the average characteristics of the slip models of past earthquakes is to compute the 2-D Fourier transforms of the slip functions of these earthquakes and analyze the resulting spatial wavenumber spectra. We derived a model for the wavenumber spectrum which falls off as the inverse of the wavenumber squared at

high wavenumbers, consistent with the model of Herrero and Bernard (1994). This wavenumber spectral model is also consistent with the stochastic fault model of Andrews (1981) and with the fractal model of Frankel (1991) when the fractal dimension is 2.

Herrero and Bernard (1994) show that the wavenumber-squared model, when combined with the assumptions of constant rupture velocity and scale-dependent rise time, results in a kinematic source model whose frequency spectrum falls off as the inverse of the frequency squared, which is the standard model of the earthquake source spectrum (Aki, 1967). Our empirical model of the wavenumber spectrum is not well constrained for wavenumbers higher than about 0.4 km^{-1}, due to the limited spatial sampling of the fault in the slip models. However, the fact that at high wavenumbers our empirical model has exactly the same decay as the theoretical model of Herrero and Bernard (1994) suggests that our wavenumber model may be reliable for higher wavenumbers.

The scaling relations of earthquake rupture models that we have developed are based on a relatively small set of events, so it is possible that they will change as new and potentially surprising information is obtained from future earthquakes. Denser networks of near-fault recording stations and improved methods of accounting for the effects of lateral variations in geological structure will be required to obtain more highly resolved images of earthquake rupture processes. This paper deals mainly with the characteristics of earthquake rupture models inferred from lowpass filtered strong motion recordings. Techniques for more adequately characterizing the seismic radiation from faults at high frequencies, such as that developed by Kaheki et al. (1996), need to be developed to provide a more reliable basis for predicting broadband ground motions for engineering design and analysis. ▨

REFERENCES

Aki, K. (1967). Scaling law of seismic spectrum, *J. Geophys. Res.* **72**, 1,217–1,231.

Andrews, D.J. (1981). A stochastic fault model, 2. Time-independent case, *J. Geophys. Res.* **86**, 10,821–10,834.

Frankel, A. (1991). High-frequency spectral falloff of earthquakes, fractal dimension of complex rupture, *b* value, and the scaling strength on fault, *J. Geophys. Res.* **96**, 6,291–6,302.

Hanks, T.C. and H. Kanamori (1979). A moment-magnitude scale, *J. Geophys. Res.* **84**, 2,348–2,350.

Hartzell, S.H. (1989). Comparison of seismic waveform inversion techniques for the rupture history of a finite fault: Application to the 1986 North Palm Springs, California, earthquake, *J. Geophys. Res.* **94**, 7,515–7,534.

Hartzell, S.H. and T.H. Heaton (1983). Inversion of strong ground motion and teleseismic waveform data for the fault rupture history of the 1979 Imperial Valley, California, earthquake, *Bull. Seism. Soc. Am.* **73**, 1,553–1,583.

Hartzell, S.H. and T.H. Heaton (1986). Rupture history of the 1984 Morgan Hill, California, earthquake from the inversion of strong motion records, *Bull. Seism. Soc. Am.* **76**, 649–674.

Hartzell, S.H. and M. Iida (1990). Source complexity of the 1987 Whittier Narrows, California, earthquake from the inversion of strong motion records, *J. Geophys. Res.* **95**, 12,475–12,485.

Hartzell, S.H., C. Langer, and C. Mendoza (1994). Rupture histories of eastern North American earthquakes, *Bull. Seism. Soc. Am.* **84**, 1,703–1,724.

Hartzell, S.H. and C. Mendoza (1991). Application of an iterative least-squares waveform inversion of strong-motion and teleseismic records to the 1978 Tabas, Iran, earthquake, *Bull. Seism. Soc. Am.* **81**, 305–331.

Hartzell, S.H., P. Liu, and C. Mendoza (1996). The 1994 Northridge, California earthquake: Investigation of rupture velocity, rise time, and high-frequency radiation, *J. Geophys. Res.* **101**, 20,091–20,108.

Heaton, T.H. (1982). The 1971 San Fernando earthquake: A double event?, *Bull. Seism. Soc. Am.* **72**, 2,037–2,062.

Heaton, T.H. (1990). Evidence for and implications of self-healing pulses of slip in earthquake rupture, *Phys. Earth Planet. Interiors* **64**, 1–20.

Herrero, A. and P. Bernard (1994). A kinematic self-similar rupture process for earthquakes, *Bull. Seism. Soc. Am.* **84**, 1,216–1,228.

Houston, H. and H. Kanamori (1986). Source spectra of great earthquakes: Teleseismic constraints on rupture process and strong motion, *Bull. Seism. Soc. Am.* **76**, 19–42.

Kamae, K. and K. Irikura (1998). Source model of the 1995 Hyogo-ken Nanbu earthquake and simulation of near-source ground motion, *Bull. Seism. Soc. Am.* **88**, 400–412.

Kaheki, Y., K. Irikura, and M. Hoshiba (1996). Estimation of high-frequency wave radiation areas on the fault plane of the 1995 Hyogo-ken Nanbu earthquake by the envelope inversion of seismograms, *J. Phys. Earth* **44**, 505–517.

Liu, H.L. and D.V. Helmberger (1983). The near-source ground motion of the 6 August 1979 Coyote Lake, California, earthquake, *Bull. Seism. Soc. Am.* **73**, 201–218.

Mendoza, C. and S.H. Hartzell (1988a). Inversion for slip distribution using GDSN P waves: North Palm Springs, Borah Peak, and Michoacán earthquakes, *Bull. Seism. Soc. Am.* **78**, 1,092–1,111.

Mendoza, C. and S. Hartzell (1988b). Aftershock patterns and mainshock faulting, *Bull. Seism. Soc. Am.* **78**, 1,438–1,449.

Shimazaki, K. (1986). Small and large earthquakes: The effect of the thickness of seismogenic layer and the free surface, Earthquake Source Mechanics, Am. Geophys. Union, *Geophys. Monogr.* **37**, 209–216.

Somerville, P.G. (1993). Engineering applications of strong ground-motion simulation, *Tectonophysics* **218**, 195–219.

Somerville, P.G., D.J. Wald, and N.F. Smith (1993). Prediction of the near-source ground accelerations of the Loma Prieta earthquake using a heterogeneous slip model. Unpublished manuscript.

Somerville, P., C.K. Saikia, D. Wald, and R. Graves (1996). Implications of the Northridge earthquake for strong ground motions from thrust faults, *Bull. Seism. Soc. Am.* **86**, S115–S125.

Tanioka, Y. and L.J. Ruff (1997). Source time functions. *Seism. Res. Lett.* **68**, 386–397.

Vidale, J.E. and D.V. Helmberger (1988). Elastic finite-difference modeling of the 1971 San Fernando, California earthquake, *Bull. Seism. Soc. Am.* **78**, 122–141.

Wald, D.J. (1996). Slip history of the 1995 Kobe, Japan, earthquake determined from strong-motion, teleseismic, and geodetic data, *J. Physics of the Earth* **44**, 489–503.

Wald, D.J., L.J. Burdick, and P.G. Somerville (1988). Simulation of acceleration time histories close to large earthquakes, *Earthquake Engineering and Soil Dynamics II: Recent Advances in Ground Motion Evaluation*, Geotechnical Special Publication 20, J. Lawrence von Thun, ed., 430–444.

Wald, D.J. and T.H. Heaton (1994). Spatial and temporal distribution of slip of the 1992 Landers, California earthquake, *Bull. Seism. Soc. Am.* **84**, 668–691.

Wald, D.J., T.H. Heaton, and K.W. Hudnut (1996). The slip history of the 1994 Northridge, California earthquake determined from strong-motion, teleseismic, GPS, and leveling data, *Bull. Seism. Soc. Am.* **86**, S49–S70.

Wald, D.J., D.V. Helmberger, and S.H. Hartzell (1990). Rupture process of the 1987 Superstition Hills earthquake from the inversion of strong-motion data, *Bull. Seism. Soc. Am.* **80**, 1,079–1,098.

Wald, D.J., D.V. Helmberger, and T.H. Heaton (1991). Rupture model of the 1989 Loma Prieta earthquake from the inversion of strong motion and broadband teleseismic data, *Bull. Seism. Soc. Am.* **81**, 1,540–1,572.

Wells, D.L. and K.J. Coppersmith (1994). Analysis of empirical relationships among magnitude, rupture length, rupture area, and surface displacement, *Bull. Seism. Soc. Am.* **84**, 974–1,002.

Woodward-Clyde Federal Services
566 El Dorado Street
Pasadena, CA 91101, U.S.A
(P.S., R.G., N.S.)

Disaster Prevention Research Institute
Kyoto University, Gokasho, Uji
Kyoto, 611-0011 Japan
(K.I., S.S.)

Pacific Gas & Electric Company
245 Market Street
San Francisco, CA 94106
(N.A.)

GeoResearch Institute
4-3-2 Itachibori, Nishi-ku
Osaka 550-0012, Japan
(Y.I., T.K.)

United States Geological Survey
525 S. Wilson Ave.
Pasadena, CA 91106
(D.W.)

6 Kansai Electric Power Co., Inc.
3-3-22, Nakanoshima, Kita-ku
Osaka, 530-8270, Japan
(A.K.)